biomolecules

MDPI

Article

Planar Boronic Graphene and Nitrogenized Graphene Heterostructure for Protein Stretch and Confinement

Xuchang Su [1,2], Zhi He [2], Lijun Meng [2], Hong Liang [1] and Ruhong Zhou [2,3,*]

[1] Department of Physics, Hangzhou Dianzi University, Hangzhou 310018, China; mr.su.su@outlook.com (X.S.); lianghongstefanie@163.com (H.L.)
[2] Institute of Quantitative Biology, College of Life Sciences, Zhejiang University, Hangzhou 310027, China; hezhi32@aliyun.com (Z.H.); ljmeng@zju.edu.cn (L.M.)
[3] Department of Chemistry, Columbia University, New York, NY 10027, USA
* Correspondence: rhzhou@zju.edu.cn

Abstract: Single-molecule techniques such as electron tunneling and atomic force microscopy have attracted growing interests in protein sequencing. For these methods, it is critical to refine and stabilize the protein sample to a "suitable mode" before applying a high-fidelity measurement. Here, we show that a planar heterostructure comprising boronic graphene (BC_3) and nitrogenized graphene (C_3N) sandwiched stripe ($BC_3/C_3N/BC_3$) is capable of the effective stretching and confinement of three types of intrinsically disordered proteins (IDPs), including amyloid-β (1–42), polyglutamine (Q42), and α-Synuclein (61–95). Our molecular dynamics simulations demonstrate that the protein molecules interact more strongly with the C_3N stripe than the BC_3 one, which leads to their capture, elongation, and confinement along the center C_3N stripe of the heterostructure. The conformational fluctuations of IDPs are substantially reduced after being stretched. This design may serve as a platform for single-molecule protein analysis with reduced thermal noise.

Keywords: molecular dynamics simulation; boronic graphene; nitrogenized graphene; inplane heterostructure; protein stretch and confinement

Citation: Su, X.; He, Z.; Meng, L.; Liang, H.; Zhou, R. Planar Boronic Graphene and Nitrogenized Graphene Heterostructure for Protein Stretch and Confinement. *Biomolecules* **2021**, *11*, 1756. https://doi.org/10.3390/biom11121756

Academic Editor: Lukasz Kurgan

Received: 29 October 2021
Accepted: 19 November 2021
Published: 24 November 2021

1. Introduction

Protein sequencing at the single-molecule level is crucial for personalized medicines and the detection of post-translational modifications in proteins [1–4]. Recently, several single-molecule techniques such as atomic force microscopy (AFM) [5,6], quantum tunneling [7–9], and nanopore [3,10,11] have been proposed for protein sequencing, which allow the direct read-out of structural differences of individual amino acids. Although promised to be with high accuracy and low cost, a large gap still resides between these proof-of-principle methods and the ultimate sensitivity for the discrimination of 20 different amino acids. One major challenge is the noisy signals caused by the thermal fluctuations of amino acids [12,13]. Moreover, proteins usually possess coiled or folded conformations in a solution, which imposes difficulties in the analysis of the atomic structure of protein [13,14]. Therefore, to put the single-molecule protein sequencers into potential commercial use, the controllable manipulation (such as elongation) and confinement of the protein conformation are prerequisites.

Current nanochannel and nanopore sequencing techniques naturally provide steric confinement for analytes, and the single-molecular sensitivity can be realized with the cross-section of confinement in the same order of magnitude as the size of the amino acids [15,16]. However, the narrow cross-section inevitably causes a large entropy barrier that hampers protein capture into the nanoscale channel [15,16]. The non-specific interaction between the protein and the nanostructure can also affect the precision of measurement and induce clogging [4,12]. To address these issues, a planar two-dimensional (2D) heterostructure has recently been proposed for biomolecular capture, stretching, and confinement [17–19]. The

planar 2D heterostructure can be fabricated by the seamless stitching of two 2D materials (for example, graphene and hexagonal boron nitride) with a similar lattice constant [20–23]. As the key mechanism for this heterostructure to manipulate protein conformation is the adsorption energy contrast for a protein molecule on different 2D materials [18,24], the performance should depend on the type of 2D material selected.

Boronic graphene (BC_3) and nitrogenized graphene (C_3N) are two new types of graphene derivatives that have been successfully synthesized [25,26]. Both BC_3 and C_3N exhibit excellent structural stability and share very similar honeycomb lattices [24,25], making them suitable to form planar heterojunctions. On the other hand, with differently doped heteroatoms (boron and nitrogen), BC_3 and C_3N have demonstrated a distinct contrast of binding affinities for biomolecules [27], which can be harnessed for biomolecular manipulation. Owing to these features, we are highly motivated to design a $BC_3/C_3N/BC_3$ in-plane heterostructure (Figure 1) for protein stretching and confinement. To study the interaction mechanism between the heterostructure and protein, three representative intrinsically disordered proteins (IDPs), including amyloid-β ($A\beta_{1–42}$), polyglutamine ($polyQ_{42}$), and α-synuclein (α-$Syn_{61–95}$) are taken as examples. Utilizing all-atom molecular dynamics (MD) simulations, we show that the disordered conformations of IDPs can be stretched into a linear manner along the C_3N stripe sandwiched between two BC_3 domains. This highly regular and confined conformation might be suitable for analysis by single-molecule methods such as AFM [5,6] and quantum tunneling [7–9]. Moreover, the conformational fluctuations of proteins can be significantly reduced after being stretched and energetically confined on the C_3N stripe. The periodic atomic charge distributions on BC_3 also induce the formation of high-density water clusters on the BC_3 surfaces, which may further provide steric hindrances to restrict the conformational fluctuation of IDPs. The insights from our study might benefit the improvement of the signal-to-noise ratio for single-molecule protein analysis.

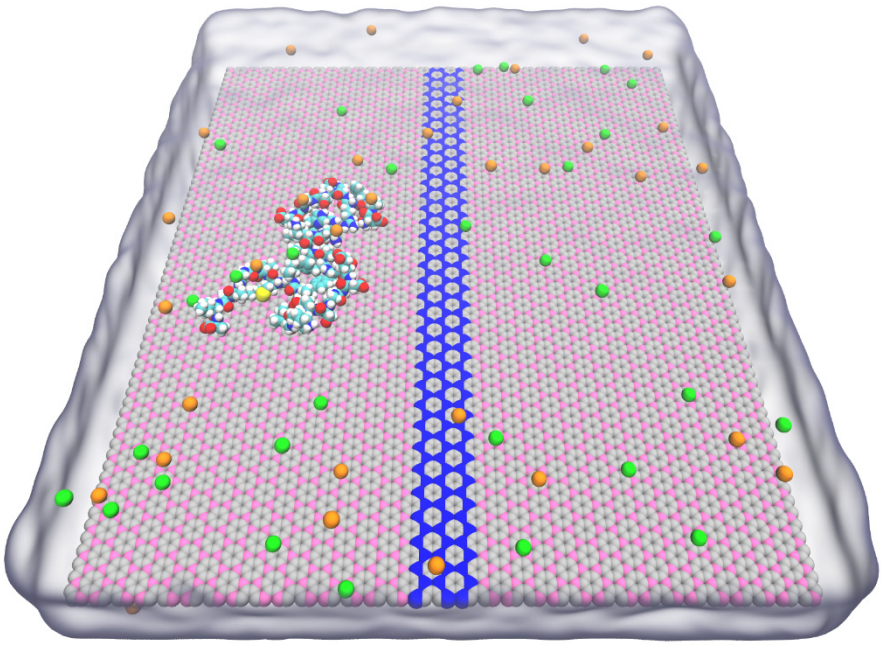

Figure 1. The initial simulation configuration of the $A\beta_{1–42}$ peptide on the $BC_3/C_3N/BC_3$ heterostructure. Carbon, boron, and nitrogen atoms in the 2D material are colored in silver, pink, and blue, respectively. Atoms in the peptide are shown as spheres (C: cyan; O: red; H: white; N: blue; and S: yellow). K^+ and Cl^- ions are colored in green and orange, while water molecules are shown as glass bubbles.

2. Method

We used molecular dynamics (MD) simulations to simulate a two-dimensional (2D) sandwich $BC_3/C_3N/BC_3$ planar heterostructure with a total size of 16.2 × 14.1 nm^2 [2] (Figure 1). Among them, the width of the C_3N stripe seamlessly spliced between the two BC_3 sheets is 1.2 nm. The force fields of BC_3 and C_3N can be obtained by referring to the previous research [28], in which the lattice constants of both are 2.5 Å, and the boron and nitrogen atoms have partial charges of 0.378 e and −0.168 e, respectively. To maintain the overall and local charge neutrality of the planar heterostructure, the carbon atoms in BC_3 and C_3N carry −0.126 e and 0.056 e, respectively [29].

Following the similar approach in our previous studies [17,24,30–32], we performed a pre-equilibrium simulation of the conformation of each IDP fragment from solution to adsorption on a BC_3 nanosheet, and then extended the BC_3 nanosheet (along with the peptide) to construct the $BC_3/C_3N/BC_3$ planar heterostructure. After that, the entire system is placed in a box with a size of 16.2 × 14.1 × 5.0 nm^3 [3] and solvated with 100 mM KCl electrolyte, which contains approximately 66,000 atoms. In addition, to explore the difference in hydrophilic or hydrophobic properties between BC_3 and C_3N, we constructed two systems of BC_3 or C_3N in a water box with a size of 4.9 × 4.2 × 5.0 nm^3 [3]. Later, to characterize the interface behavior of water molecules on the planar heterostructure, we additionally constructed a heterostructure-water system with a box size of 16.2 × 14.1 × 5.0 nm^3 [3].

The Gromacs software package [33] (version 5.1.4) was used for our MD simulations, and VMD [34] was used for trajectory visualization. The TIP3P model [35] was used for water molecules, the CHARMM36 force field [36] for proteins/peptides, and standard force fields for ions. Following the scheme used in many previous, similar researches [30,37–41], we used the LINCS algorithm to constrain the covalent bonds with hydrogen atoms, with a time step of 2 fs. The particle mesh Ewald (PME) method [42] with a grid size of about 1 Å was used to calculate the long-range electrostatic interactions, while the smooth cut-off method was used for the van der Waals (vdW) interactions, with a cut-off distance of 1.2 nm. Periodic boundary conditions were used in all three-dimensional directions. The Parrinello-Rahman algorithm [43] was applied in the z-direction with a semi-isotropic pressure coupling of 1 bar, and the V-rescale thermostat [44] was used to control the simulation temperature at 300 K. Then, under the NPT ensemble, several independent 400 ns trajectories were generated for each system for data collection. In all simulations, except that the atoms in the two-dimensional planar heterostructure are frozen, all other atoms can move freely.

3. Result

Some representative snapshots (Figure 2) were shown for the trajectories of Aβ, polyQ, and α-Syn on the $BC_3/C_3N/BC_3$ planar heterojunction, respectively. Taking Aβ (Figure 2A) as an example, starting from the curled and folded structure adsorbed on the BC_3 domain, Aβ first diffused to the C_3N region quickly, arriving at t = ~22 ns, which is consistent with our previous findings on the similar free and rapid diffusions of adsorbents on other two-dimensional material plane [24]. Finally, at t = ~250 ns, Aβ was stretched on the C_3N stripe and maintains a straightened conformation. Following the same procedure, we also checked the trajectories of polyQ (Figure 2B) and α-Syn (Figure 2C) and found that although they had slightly different dynamic behaviors in the initial diffusion and subsequent stretching phases, they all displayed the same straightened conformation as Aβ on the C_3N stripe at the end. In addition, we analyzed the average end-to-end distance normalized by the residue number (*L/N*) for each protein (Figure 2D). During the simulation, the *L/N* of Aβ, polyQ, and α-Syn increased from ~1.0 Å to 2.2 Å, 2.2 Å, and 2.3 Å, respectively. It is worth noting that although the *L/N* values of these IDPs fluctuate sharply due to their high flexibility before being fully stretched, they maintain their respective highest values during the last 100 ns simulations, indicating that IDPs can be spontaneously stretched on the C_3N stripe. It is also worth noting that the fluctuations

of *L/N* are reduced after the peptides are stretched (Figure 2D). To characterize the change of conformational fluctuations of peptides in the stretching process, we further conducted MD simulations of peptides in free solution, on the BC_3 surface, and the $BC_3/C_3N/BC_3$ surface, respectively. Figure 3 illustrates the probability distributions of *L/N* of Aβ peptides in different environments. The distribution of *L/N* of Aβ confined in the heterostructure has a much narrower width than those in other environments. Moreover, distributions of *L/N* of polyQ (Figure S1) and a-Syn (Figure S2) also demonstrate similar results. The above analyses indicate that the conformational fluctuations of proteins can be significantly reduced when they are confined on the C_3N stripe $BC_3/C_3N/BC_3$.

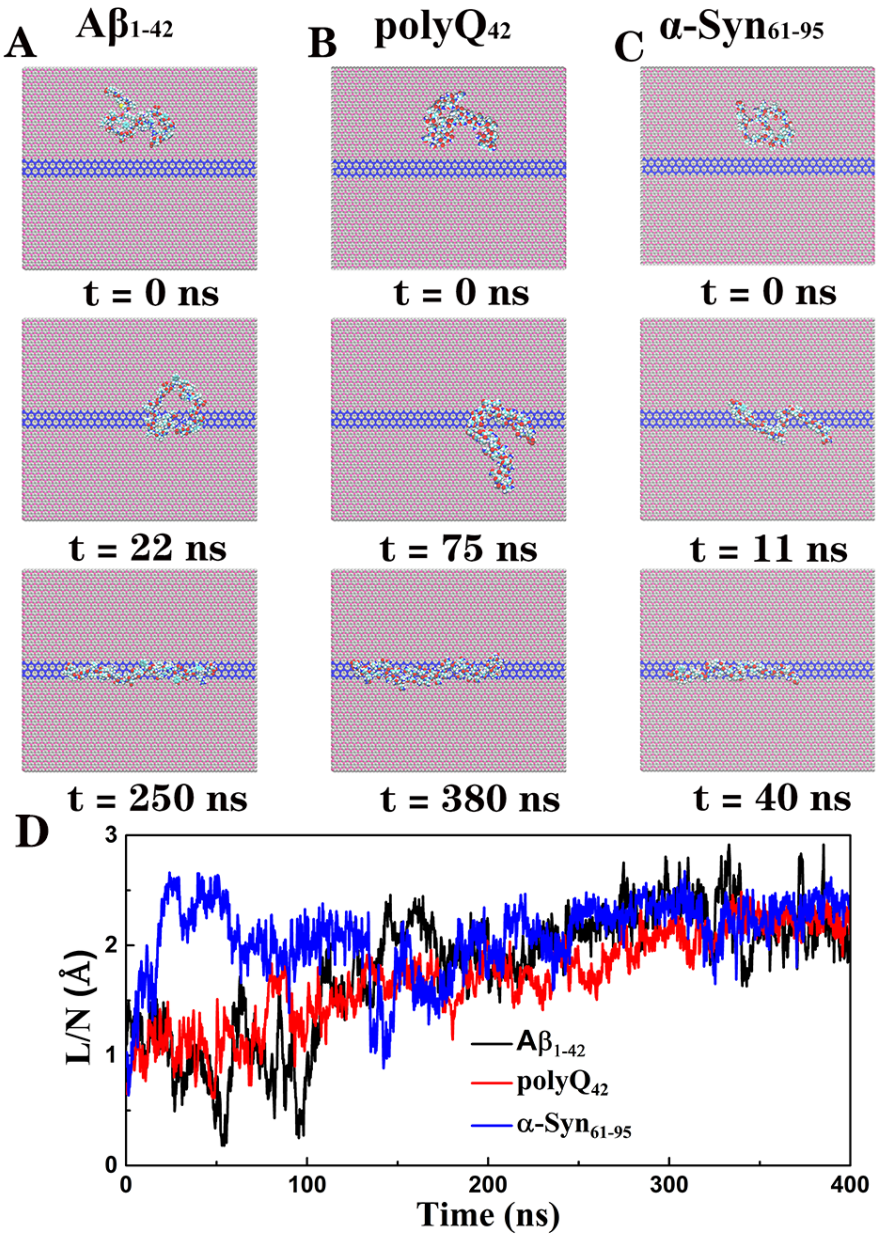

Figure 2. Representative snapshots of stretching processes of (**A**) $A\beta_{1–42}$, (**B**) $polyQ_{42}$, and (**C**) α-$Syn_{61–95}$ on $BC_3/C_3N/BC_3$. (**D**) End-to-end distances for Aβ (black line), polyQ (red line), α-Syn (blue line) during the simulations.

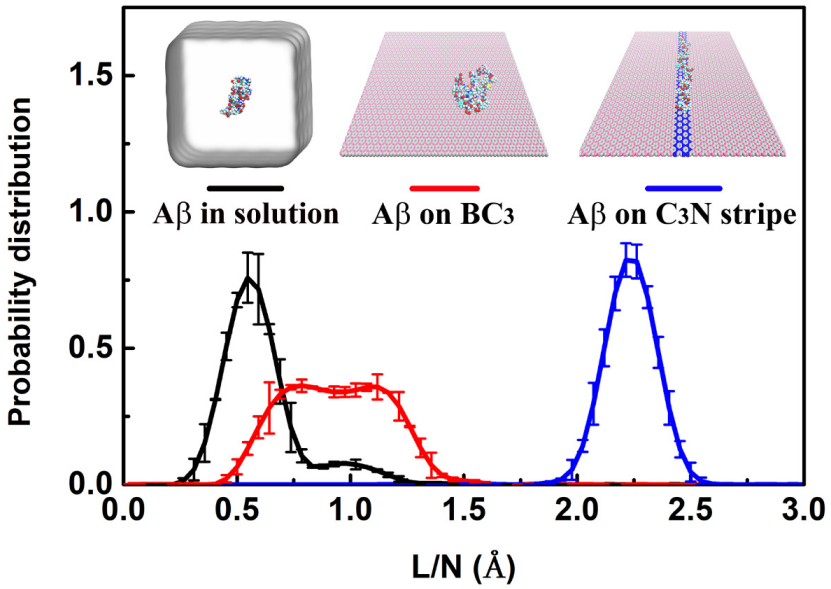

Figure 3. Probability distribution of end-to-end distances for Aβ in solution (black line), on BC_3 surface (red line), and on C_3N stripe (blue line).

To reveal the stretching mechanism of IDPs on the $BC_3/C_3N/BC_3$ planar heterostructure, we adopted Aβ as an example to examine the details of the interaction between peptides and $BC_3/C_3N/BC_3$ (Figure 4). During the simulation, the average number of contact atoms per Aβ residue with BC_3 decreased from ~9 to ~4, while the average number of contact atoms per Aβ residue with C_3N increased from 0 to ~8 (Figure 4A). Here, we defined a contact when any atom in $BC_3/C_3N/BC_3$ was within 4.0 Å of any heavy atom of the protein. As shown in the scatter plot of Figure 4B, in the stretching process, the peptide contacted more with C_3N while less with BC_3, accompanied by a gradual increase in the magnitude of interaction energy. According to the above results, the peptide interacted more strongly with C_3N than BC_3, which drove its stretching on $BC_3/C_3N/BC_3$. To further understand the physical mechanism of the driven process, we scanned the interaction energy ΔE between the peptide and $BC_3/C_3N/BC_3$ by moving the stretched conformation of Aβ horizontally and rigidly from the C_3N stripe to the BC_3 domain. As shown in Figure 4C, when the peptide was on the C_3N stripe, the van der Waals interaction (vdW) energy presented a narrow energy well with a depth of −1.6 kcal per mol per residue (black dotted line). It is also worth noting that the average value of Coulomb interaction energy between Aβ and the $BC_3/C_3N/BC_3$ was almost zero (red line) due to the local charge neutrality of the planar heterostructure. Moreover, we repeated all of the above analyses for the polyQ (Figure S3) and α-Syn (Figure S4) on $BC_3/C_3N/BC_3$. Similarly, the straightening and restriction of polyQ and α-Syn on the narrow C_3N stripe were also mainly due to the differences in the vdW interactions between the polypeptides and C_3N and BC_3.

To further investigate the influence of the C_3N stripe width on the efficiency of protein stretching, we also constructed $BC_3/C_3N/BC_3$ heterostructures with the stripe widths ranging from 0.6 nm to 1.8 nm and scanned the vdW interaction energy between the elongated Aβ peptide and each heterostructure, respectively (Figure S5). Figure S5B shows the potential wells of C_3N stripes with different widths, and Figure S5C shows the "potential-depth" and the "potential-width" at a half-minimum of each well as a function of the C_3N stripe width. For both curves of the depths and widths of potential wells, the inflection points occur when the C_3N layer width is equal to 1.2 nm. After this deflection point, the increasing stripe width would lead to a slower decrease of the depth of the potential well, and a faster increase of the width of the potential well. It is noteworthy that a potential well with a deeper depth and narrower width can lead to a better performance of the protein stretching. Considering the optimization of both the depth and the width

of the potential well, the C_3N layer width of 1.2 nm is recommended for efficient protein stretching.

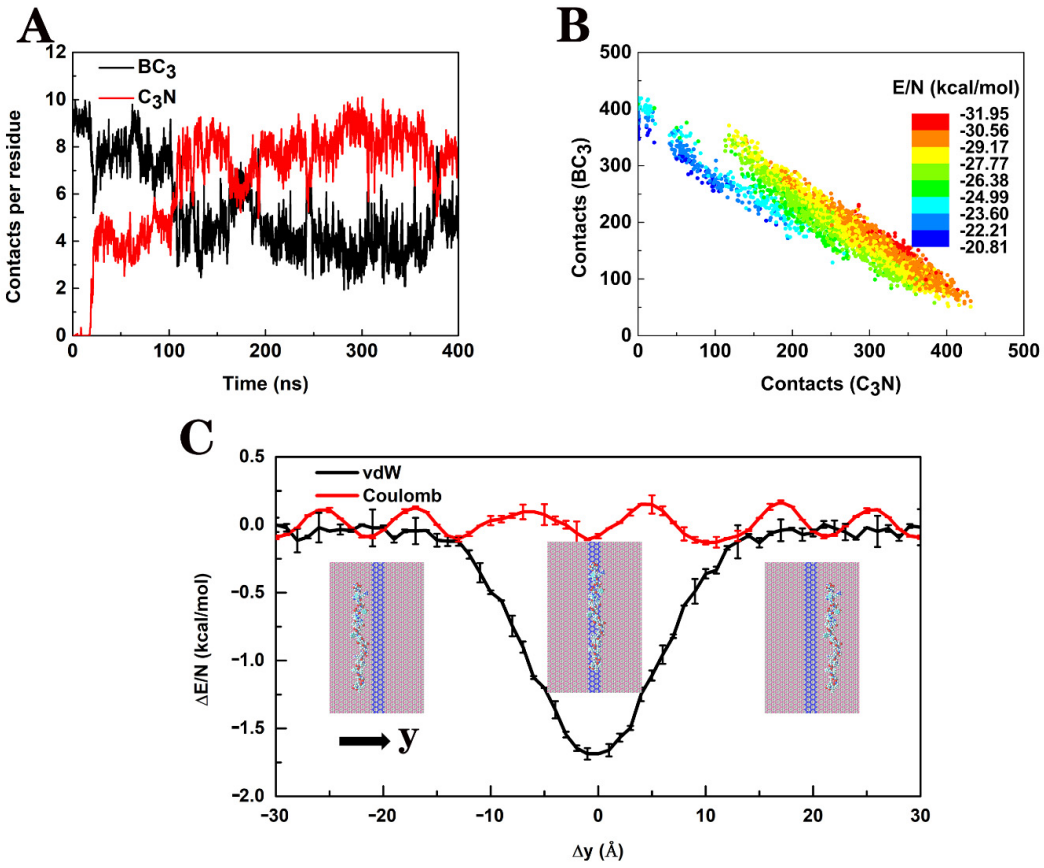

Figure 4. (**A**) Number of atoms in $BC_3/C_3N/BC_3$ that are within 4.0 Å of the Aβ peptide throughout the simulation. (**B**) A scatter plot of the number of atoms in $BC_3/C_3N/BC_3$ in contact with Aβ. The color represents the average interaction energy per residue between Aβ and $BC_3/C_3N/BC_3$. (**C**) The average van der Waals (black line) and Coulomb (red line) interaction energy between Aβ and $BC_3/C_3N/BC_3$ with standard deviations, when the elongated Aβ peptide moved across the C_3N band in the y-direction.

Moreover, in practice, the interface between BC_3 and C_3N may not be perfect, as shown in Figure 1, and rough domains with mixed units of BC_3 and C_3N might exist at the interface. One simple way to illustrate this effect is to use the 1.2-nm-width C_3N stripe in our current simulation as the base and use the width of the 1.0-nm- to 1.4-nm-C_3N stripes as the upper and lower bounds, as the adsorption potential well of the stripe with rough interfaces should be in-between the wells of these two widths. As shown above in Figure S5B, the potential wells of the 1.0-nm-width, 1.2-nm-width, and 1.4-nm-width C_3N stripes share similar shapes, with potential-well depths of −1.4 kcal/mol, −1.6 kcal/mol, and −1.7 kcal/mol respectively. Thus, the roughness of the interface is not likely to affect much on the potential well for protein stretching and confinement.

In addition, it is known that the behavior of water on the surface of 2D materials also has an important influence on the interaction between protein and 2D materials in the aqueous environment. Therefore, we further analyzed the behaviors of interfacial water on BC_3 and C_3N respectively, and the influence of these interfacial waters on the confinement of IDPs on the planar heterostructure (Figure 5). From the water density maps (Figure 5A,B) along the normal (Z) directions of 2D materials, the first water solvation shells of BC_3 and C_3N were both located on $Z = \pm 0.35$ nm. More interestingly, we found a periodic enhancement of water density clusters between the BC_3 layer and its first solvation shell, which were not observed clearly on the C_3N layer. The presence of these water clusters on

BC_3 might be attributed to the strong but nonuniform partial charge distributions (+0.378 e for a boron atom and −0.126 e for a carbon atom). While on C_3N, the partial charges (−0.168 e for a carbon atom and +0.056 e for a nitrogen atom) were much smaller, and not strong enough to induce noticeable water clusters between the 2D layer and the first solvation shell. Meanwhile, we further calculated the two-dimensional water density map along the surface (*XY* direction) of $BC_3/C_3N/BC_3$ (only water molecules within 0.25 nm in the *Z* direction of the 2D plane were counted). As shown in Figure 5C,D, these water clusters were periodically distributed on the BC_3 domain, which could form a steric hindrance (Figure 5E) that hindered the diffusion of IDPs' residues to the BC_3 domain. These interfacial water molecules might further strengthen the restriction on the linear conformation of IDPs.

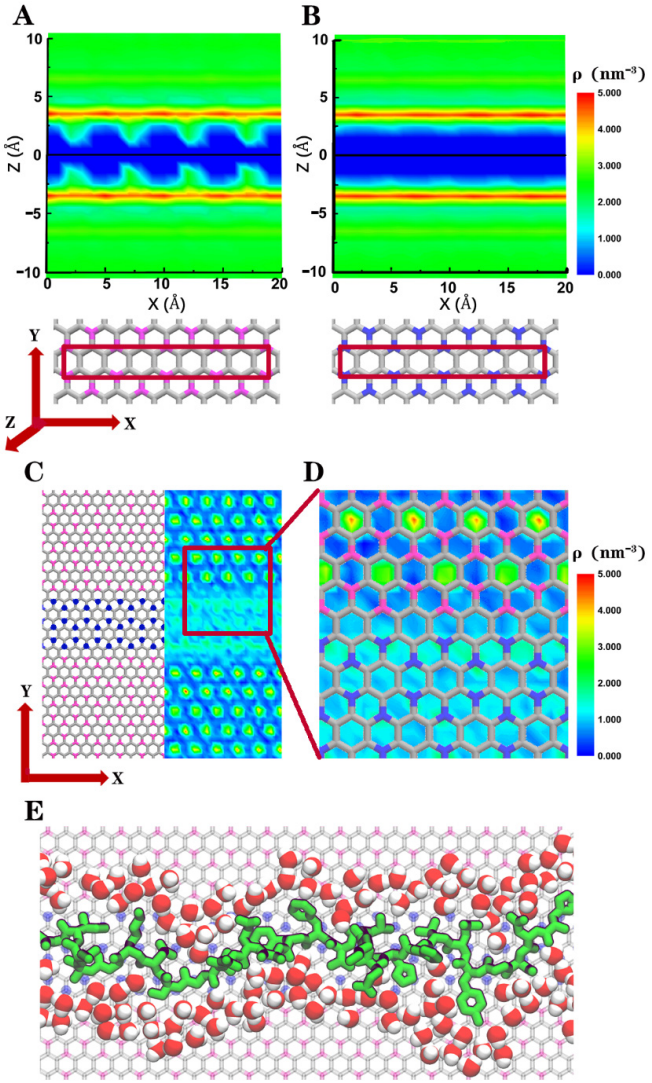

Figure 5. The density maps of water along the normal directions of the (**A**) BC_3 and (**B**) C_3N planes, where the 2D materials are located at Z = 0. As shown in the structure below, the calculation was performed along the zigzag direction, while only water molecules inside the red square were calculated. (**C**) Two-dimensional water density map on the $BC_3/C_3N/BC_3$ surface; water molecules within ±0.25 nm in the *Z* direction were counted. (**D**) Magnified map of water density at the boundary of BC_3 and C_3N. (**E**) Straightened Aβ peptide on $BC_3/C_3N/BC_3$ with interfacial water surrounded; only water molecules within 0.5 nm of both the heterostructure and protein are shown.

4. Conclusions

In this work, we applied molecular dynamics (MD) simulation to study the stretching process of several representative IDPs on the 2D sandwiched $BC_3/C_3N/BC_3$ planar heterostructure. The IDPs could be spontaneously straightened and then restricted along the C_3N stripes. Moreover, we have shown that the conformational fluctuations of IDPs were significantly reduced when IDPs were confined on the C_3N stripe. The protein stretching and confinement were mainly driven by the stronger adsorption potential of C_3N than that of BC_3. Additionally, we found that the interfacial water molecules on the BC_3 surface might further act as steric hindrances to enhance the restriction of protein. This linearly confined structure on the 2D surface may be feasible for scanning tunneling microscope (STM) [45,46] and atomic force microscope (AFM) [5,6] to identify the amino acids in the protein. Furthermore, compared with other "hard" nano-confinements such as nanochannels and nanopores, this heterostructure provides "soft" confinement that is based on the adsorption potential difference between the two 2D nanomaterials. Considering the large entropy barrier for stretching a coiled or folded protein to a linear conformation, this soft, energetic confinement allows some protein residues to temporarily move outside the center C_3N stripe while "regulating" the protein conformation, thus smoothly overcoming the entropy barrier in the stretching process. Therefore, this heterostructure holds the potential to be coupled with nanopore- and nanochannel-sensing methods to ease the clogging problem. The delivery of the stretched protein samples from this heterostructure to a nanochannel can be driven by a pressure-driven flow, for example. Last but not least, C_3N and BC_3 have been reported to possess higher biocompatibility than graphene [28]. Our work may also offer insight into the design of biocompatible nanodevices.

Supplementary Materials: The following are available online at https://www.mdpi.com/article/10.3390/biom11121756/s1, Figure S1: Analysis of end-to-end distances for polyglutamine ($polyQ_{42}$) in solution, on boronic graphene (BC_3), and the nitrogenized graphene (C_3N) stripe. Figure S2: Analysis of end-to-end distances for α-Synuclein (α-$Syn_{61–95}$) in solution, on BC_3, and the C_3N stripe, Figure S3: Detailed analysis of the $polyQ_{42}$ stretching process on the $BC_3/C_3N/BC_3$ heterostructure, Figure S4: Detailed analysis of the α-$Syn_{61–95}$ stretching process on the $BC_3/C_3N/BC_3$ heterostructure, Figure S5: Influence of the C_3N stripe width on the potential well for the straightened Aβ peptide.

Author Contributions: Conceptualization, Z.H. and R.Z.; methodology, X.S. and Z.H.; software, X.S.; validation, Z.H., H.L. and R.Z.; formal analysis, X.S.; investigation, X.S. and Z.H.; resources, R.Z.; data curation, Z.H.; writing—original draft preparation, X.S.; writing—review and editing, Z.H. and L.M. and R.Z.; visualization, X.S.; supervision, H.L. and R.Z.; project administration, R.Z.; funding acquisition, R.Z. All authors have read and agreed to the published version of the manuscript.

Funding: This work is partially supported by the National Natural Science Foundation of China (Grants U1967217 and 11574224), the National Independent Innovation Demonstration Zone Shanghai Zhangjiang Major Projects (ZJZX2020014), and the Starry Night Science Fund of Zhejiang University Shanghai Institute for Advanced Study (SN-ZJU-SIAS-003). R.Z. also acknowledges the financial support from W. M. Keck Foundation (Grant award 2019-2022).

Institutional Review Board Statement: Not applicable.

Informed Consent Statement: Not applicable.

Data Availability Statement: Not applicable.

Acknowledgments: We would like to thank Jianxiang Huang, Wei Song, David Bell, and Dong Zhang for helpful discussions of the manuscript.

Conflicts of Interest: The authors declare no conflict of interest.

References

1. Yao, Y.; Docter, M.; Ginkel, J.V.; Ridder, D.D.; Joo, C. Single-molecule protein sequencing through fingerprinting: Computational assessment. *Phys. Biol.* **2015**, *12*, 055003. [CrossRef] [PubMed]
2. Filius, M.; Ginkel, J.V.; Joo, C. Engineering ClpXP for single-molecule protein sequencing. *Biophys. J.* **2017**, *112*, 151a. [CrossRef]

3. Brinkerhoff, H.; Kang, A.S.; Liu, J.; Aksimentiev, A.; Dekker, C. Multiple rereads of single proteins at single–amino acid resolution using nanopores. *Science* **2021**, eabl4381. [CrossRef] [PubMed]
4. Alfaro, J.A.; Bohländer, P.; Dai, M.; Filius, M.; Howard, C.J.; van Kooten, X.F.; Ohayon, S.; Pomorski, A.; Schmid, S.; Aksimentiev, A. The emerging landscape of single-molecule protein sequencing technologies. *Nat. Methods* **2021**, *18*, 604–617. [CrossRef] [PubMed]
5. Gross, L.; Mohn, F.; Moll, N.; Liljeroth, P.; Meyer, G. The chemical structure of a molecule resolved by atomic force microscopy. *Science* **2009**, *325*, 1110–1114. [CrossRef] [PubMed]
6. Fatayer, S.; Albrecht, F.; Zhang, Y.; Urbonas, D.; Pena, D.; Moll, N.; Gross, L. Molecular structure elucidation with charge-state control. *Science* **2019**, *365*, 142–145. [CrossRef] [PubMed]
7. Morikawa, T.; Yokota, K.; Tsutsui, M.; Taniguchi, M. Fast and low-noise tunnelling current measurements for single-molecule detection in an electrolyte solution using insulator-protected nanoelectrodes. *Nanoscale* **2017**, *9*, 4076–4081. [CrossRef] [PubMed]
8. Ventra, M.; Taniguchi, M. Decoding DNA, RNA and peptides with quantum tunnelling. *Nat. Nanotechnol.* **2016**, *11*, 117–126. [CrossRef]
9. Ohshiro, T.; Tsutsui, M.; Yokota, K.; Furuhashi, M.; Taniguchi, M.; Kawai, T. Detection of post-translational modifications in single peptides using electron tunnelling currents. *Nat. Nanotechnol.* **2014**, *9*, 835–840. [CrossRef]
10. Yusko, E.C.; Bruhn, B.R.; Eggenberger, O.M.; Houghtaling, J.; Rollings, R.C.; Walsh, N.C.; Nandivada, S.; Pindrus, M.; Hall, A.R.; Sept, D. Real-time shape approximation and fingerprinting of single proteins using a nanopore. *Nat. Nanotechnol.* **2017**, *12*, 360–367. [CrossRef]
11. Ouldali, H.; Sarthak, K.; Enslen, T.; Piguet, F.; Manivet, P.; Pelta, J.; Behrends, J.C.; Aksimentiev, A.; Oukhaled, A. Electrical recognition of the twenty proteinogenic amino acids using an aerolysin nanopore. *Nat. Biotechnol.* **2020**, *38*, 176–181. [CrossRef]
12. Domon, B.; Aebersold, R. Options and considerations when selecting a quantitative proteomics strategy. *Nat. Biotechnol.* **2010**, *28*, 710–721. [CrossRef] [PubMed]
13. Laura, R.-P.; Chirlmin, J.C.; Dekker, C. Paving the way to single-molecule protein sequencing. *Nat. Nanotechnol.* **2018**, *13*, 786–796.
14. Uversky, V.N. A decade and a half of protein intrinsic disorder: Biology still waits for physics. *Protein Sci.* **2013**, *22*, 693–724. [CrossRef] [PubMed]
15. Muthukumar, M. Translocation of a confined polymer through a hole. *Phys. Rev. Lett.* **2001**, *86*, 3188–3191. [CrossRef] [PubMed]
16. Zhou, J.; Wang, Y.; Menard, L.D.; Panyukov, S.; Rubinstein, M.; Ramsey, J.M. Enhanced nanochannel translocation and localization of genomic DNA molecules using three-dimensional nanofunnels. *Nat. Commun.* **2017**, *8*, 807. [CrossRef]
17. Luan, B.; Zhou, R. Spontaneous ssDNA stretching on graphene and hexagonal boron nitride in plane heterostructures. *Nat. Commun.* **2019**, *10*, 4610. [CrossRef] [PubMed]
18. Luan, B. Energetically stretching proteins on patterned two-dimensional nanosheets. *Nano Futures* **2020**, *4*, 035001. [CrossRef]
19. He, Z.; Zhou, R. Exploring in-plane graphene and hexagonal boron nitride array for separation of single nucleotides. *ACS Nano* **2021**, *15*, 11704–11710. [CrossRef]
20. Duan, X.; Chen, W.; Shaw, J.C.; Rui, C.; Chen, Y.; Li, H.; Wu, X.; Tang, Y.; Zhang, Q.; Pan, A. Lateral epitaxial growth of two-dimensional layered semiconductor heterojunctions. *Nat. Nanotechnol.* **2014**, *9*, 1024–1030. [CrossRef]
21. Huang, C.; Wu, S.; Sanchez, A.M.; Peters, J.; Beanland, R.; Rivera, P.; Yao, W.; Cobden, D.H.; Xu, X. Lateral heterojunctions within monolayer semiconductors. *Nat. Mater.* **2014**, *13*, 1096–1101. [CrossRef] [PubMed]
22. Zhang, C.; Li, M.-Y.T. Strain distributions and their influence on electronic structures of WSe2-MoS2 laterally strained heterojunctions. *Nat. Nanotechnol.* **2018**, *13*, 152–158. [CrossRef] [PubMed]
23. Wang, H.S.; Chen, L.; Elibol, K.; He, L.; Wang, H.; Chen, C.; Jiang, C.; Li, C.; Wu, T.; Cong, C.X. Towards chirality control of graphene nanoribbons embedded in hexagonal boron nitride. *Nat. Mater.* **2021**, *20*, 202–207. [CrossRef] [PubMed]
24. He, Z.; Zhou, R. Planar graphene/h-BN/graphene heterostructures for protein stretching and confinement. *Nanoscale* **2020**, *12*, 13822–13828. [CrossRef]
25. Bohayra, M. Ultra-high stiffness and thermal conductivity of graphene-like C3N. *Carbon* **2017**, *118*, 25–34.
26. King, T.C.; Matthews, P.D.; Glass, H.; Cormack, J.A.; Holgado, J.P.; Leskes, M.; Griffin, J.M.; Scherman, O.A.; Barker, P.D.; Grey, C.P. Theory and Practice: Bulk synthesis of C3B and its H2- and Li-storage capacity. *Angew. Chem. Int. Ed.* **2015**, *127*, 6017–6021. [CrossRef]
27. Wang, Y.; Shao, Y.; Matson, D.W.; Li, J.; Lin, Y. Nitrogen-doped graphene and its application in electrochemical biosensing. *ACS Nano* **2010**, *4*, 1790–1798. [CrossRef]
28. Deng, Y.; Wang, F.; Liu, Y.; Yang, Y.; Li, W. Orientational binding and directional transport of DNA on nanomaterial heterojunctions. *Nanoscale* **2020**, *12*, 5217–5226. [CrossRef]
29. Chen, Y.; Wu, Y.; Sun, B.; Liu, S.; Liu, H. Two-dimensional nanomaterials for cancer nano-theranostics. *Small* **2017**, *13*, 1603446. [CrossRef]
30. Tu, Y.; Lv, M.; Xiu, P.; Huynh, T.; Zhang, M.; Castelli, M.; Liu, Z.; Huang, Q.; Fan, C.; Fang, H. Destructive extraction of phospholipids from Escherichia coli membranes by graphene nanosheets. *Nat. Nanotechnol.* **2013**, *8*, 594–601. [CrossRef]
31. Ahmed, R.; Omidian, Z.; Giwa, A.; Cornwell, B.; Majety, N.D.R.; Lee, S.; Zhang, H.; Michels, A.; Desiderio, S. A public BCR present in a unique dual-receptor-expressing lymphocyte from type 1 diabetes patients encodes a potent T cell autoantigen. *Cell* **2019**, *177*, 1583–1599. [CrossRef] [PubMed]

32. Binquan, L.; Ruhong, Z. Atomic-scale fluidic diodes based on triangular nanopores in bilayer hexagonal boron nitride. *Nano Lett.* **2019**, *19*, 977–982.
33. Pronk, S.; Páll, S.; Schulz, R.; Larsson, P.; Bjelkmar, P.; Apostolov, R.; Shirts, M.R.; Smith, J.C.; Kasson, P.M.; Van Der Spoel, D. Gromacs 4.5: A high-throughput and highly parallel open source molecular simulation toolkit. *Bioinformatics* **2013**, *29*, 845–854. [CrossRef] [PubMed]
34. Humphrey, W.; Dalke, A.; Schulten, K. Vmd: Visual molecular dynamics. *J. Mol. Graph.* **1996**, *14*, 33–38. [CrossRef]
35. Jamsawang, P. Comparison of simple potential functions for simulating liquid water. *J. Chem. Phys.* **2018**, *79*, 926–935.
36. Foloppe, N.; Mackerell, A.D. All-atom empirical force field for nucleic acids: I. Parameter optimization based on small molecule and condensed phase macromolecular target data. *J. Comput. Chem.* **2000**, *21*, 86–104. [CrossRef]
37. Giampaga, M.; Zhestkov, Y.; Pitman, M.; Suits, F.; Grossfield, A.; Zhestkov, Y.; Pitman, M.C.; Suits, F.; Grossfield, A.; Pitera, J. Blue matter: Strong scaling of molecular dynamics on blue gene/L. In *International Conference on Computational Science*; Springer: Berlin/Heidelberg, Germany, 2006.
38. Kaminski, G.A.; Friesner, R.A.; Zhou, R. A computationally inexpensive modification of the point dipole electrostatic polarization model for molecular simulations. *J. Comput. Chem.* **2003**, *24*, 267. [CrossRef]
39. Zhou, R. Hydrophobic collapse in multidomain protein folding. *Science* **2004**, *305*, 1605–1609. [CrossRef] [PubMed]
40. Luo, N.; Weber, J.K.; Wang, S.; Luan, B.; Yue, H.; Xi, X.; Du, J.; Yang, Z.; Wei, W.; Zhou, R. Pegylated graphene oxide elicits strong immunological responses despite surface passivation. *Nat. Commun.* **2017**, *8*, 14537. [CrossRef]
41. Chowell, D.; Morris, L.G.; Grigg, C.M.; Weber, J.K.; Samstein, R.M.; Makarov, V.; Kuo, F.; Kendall, S.M.; Requena, D.; Riaz, N. Patient HLA class I genotype influences cancer response to checkpoint blockade immunotherapy. *Science* **2018**, *359*, 582–587. [CrossRef] [PubMed]
42. Darden, T.; York, D.; Pedersen, L. Particle mesh ewald: An N·log(N) method for ewald sums in large systems. *J. Chem. Phys.* **1993**, *98*, 10089–10092. [CrossRef]
43. Rahman, A. Polymorphic transitions in single crystals: A new molecular dynamics method. *J. Appl. Phys.* **1981**, *52*, 7182.
44. Bussi, G.; Donadio, D.; Parrinello, M. Canonical sampling through velocity rescaling. *J. Chem. Phys.* **2007**, *126*, 014101. [CrossRef] [PubMed]
45. Huang, S.; He, J.; Chang, S.; Zhang, P.; Liang, F.; Li, S.; Tuchband, M.; Fuhrmann, A.; Ros, R.; Lindsay, S. Identifying single bases in a DNA oligomer with electron tunnelling. *Nat. Nanotechnol.* **2010**, *5*, 868–873. [CrossRef]
46. Tanaka, H.; Kawai, T. Partial sequencing of a single DNA molecule with a scanning tunneling microscope. *Nat. Nanotechnol.* **2009**, *4*, 518–522. [CrossRef]